

## High-sensitivity Q-band electron spin resonance imaging system with submicron resolution

Lazar Shtirberg, Ygal Twig, Ekaterina Dikarov, Revital Halevy, Michael Levit et al.

Citation: *Rev. Sci. Instrum.* **82**, 043708 (2011); doi: 10.1063/1.3581226

View online: <http://dx.doi.org/10.1063/1.3581226>

View Table of Contents: <http://rsi.aip.org/resource/1/RSINAK/v82/i4>

Published by the [American Institute of Physics](http://www.aip.org).

---

### Related Articles

Terahertz scattering by two phased media with optically soft scatterers

*J. Appl. Phys.* **112**, 113112 (2012)

A single coil radio frequency gradient probe for nuclear magnetic resonance applications

*Rev. Sci. Instrum.* **83**, 124701 (2012)

GaP based terahertz time-domain spectrometer optimized for the 5-8 THz range

*Appl. Phys. Lett.* **101**, 181101 (2012)

On the performance enhancement of adaptive signal averaging: A means for improving the sensitivity and rate of data acquisition in magnetic resonance and other analytical measurements

*Rev. Sci. Instrum.* **83**, 105108 (2012)

Terahertz detection by heterostructured InAs/InSb nanowire based field effect transistors

*Appl. Phys. Lett.* **101**, 141103 (2012)

---

### Additional information on Rev. Sci. Instrum.

Journal Homepage: <http://rsi.aip.org>


Journal Information: [http://rsi.aip.org/about/about\\_the\\_journal](http://rsi.aip.org/about/about_the_journal)

Top downloads: [http://rsi.aip.org/features/most\\_downloaded](http://rsi.aip.org/features/most_downloaded)

Information for Authors: <http://rsi.aip.org/authors>

## ADVERTISEMENT

**JANIS** Does your research require low temperatures? Contact Janis today.  
Our engineers will assist you in choosing the best system for your application.



10 mK to 800 K      LHe/LN<sub>2</sub> Cryostats  
Cryocoolers      Magnet Systems  
Dilution Refrigerator Systems  
Micro-manipulated Probe Stations

[sales@janis.com](mailto:sales@janis.com)      [www.janis.com](http://www.janis.com)  
Click to view our product web page.

# High-sensitivity Q-band electron spin resonance imaging system with submicron resolution

Lazar Shtirberg, Ygal Twig, Ekaterina Dikarov, Revital Halevy, Michael Levit, and Aharon Blank<sup>a)</sup>

Schulich Faculty of Chemistry, Technion – Israel Institute of Technology, Haifa 32000, Israel

(Received 6 February 2011; accepted 28 March 2011; published online 22 April 2011)

A pulsed electron spin resonance (ESR) microimaging system operating at the Q-band frequency range is presented. The system includes a pulsed ESR spectrometer, gradient drivers, and a unique high-sensitivity imaging probe. The pulsed gradient drivers are capable of producing peak currents ranging from  $\sim 9$  A for short 150 ns pulses up to more than 94 A for long 1400 ns gradient pulses. Under optimal conditions, the imaging probe provides spin sensitivity of  $\sim 1.6 \times 10^8$  spins/ $\sqrt{\text{Hz}}$  or  $\sim 2.7 \times 10^6$  spins for 1 h of acquisition. This combination of high gradients and high spin sensitivity enables the acquisition of ESR images with a resolution down to  $\sim 440$  nm for a high spin concentration solid sample ( $\sim 10^8$  spins/ $\mu\text{m}^3$ ) and  $\sim 6.7$   $\mu\text{m}$  for a low spin concentration liquid sample ( $\sim 6 \times 10^5$  spins/ $\mu\text{m}^3$ ). Potential applications of this system range from the imaging of point defects in crystals and semiconductors to measurements of oxygen concentration in biological samples. © 2011 American Institute of Physics. [doi:10.1063/1.3581226]

## I. INTRODUCTION

Electron spin resonance (ESR) is a powerful spectroscopic method employed in the study of free radicals, crystal defects, and transient paramagnetic species. ESR is used extensively in the fields of science ranging from physics to biology and from medicine to materials science. In the case of heterogeneous samples one is often required to provide ESR spectra or other ESR-related information (such as spins concentration, relaxation times,<sup>1</sup> or even ESR-derived diffusion<sup>2,3</sup>) in a spatially resolved manner. This is achieved by means of ESR imaging systems. The basic physical principles of ESR imaging are similar to the more common nuclear magnetic resonance (NMR) imaging [often referred to as magnetic resonance imaging–MRI]. The main differences, however, are the time scales (nanoseconds up to microseconds in ESR versus milliseconds in NMR), the operating frequency ( $\sim$ GHz and tens of GHz in ESR versus hundreds of MHz in NMR), and the spin sensitivity (roughly 5–6 orders of magnitude larger in ESR than NMR). (These comparative parameters are, of course, dependent upon the specific experimental setup, sample type and environmental conditions,<sup>4,5</sup> and are thus listed here only for general impression). Most ESR imaging work is carried out with *ex vivo* isolated organs or *in vivo* small animals (rats and mice) looking at exogenous radicals with millimeter-scale resolution.<sup>6–8</sup> However, there are many applications in which much smaller samples are involved, which in turn require a much higher sensitivity and higher spatial resolution in the micrometer scale and even below that.<sup>9</sup> Such applications are, for example, oxygen imaging in and around cells,<sup>10</sup> imaging of defects in semiconductors,<sup>11</sup> observation of material distribution and diffusion in microspheres,<sup>12</sup> and in

the more distant future, possibly even imaging of individual spins for quantum computing applications.<sup>13</sup>

Recently, we were involved in the development of high-spin-sensitivity high-resolution ESR microscopy systems, which are aimed at approaching exactly these kinds of applications.<sup>9,14–17</sup> These systems operate both in pulsed<sup>15</sup> and continuous wave (CW) modes<sup>17</sup> at room temperature. While the CW systems are best suited for radicals having very short relaxation times ( $T_2 < 100$  ns), pulse ESR imaging is more useful for radicals having long  $T_2$ . With pulse system, one can achieve better sensitivity and resolution, collect the image much faster, and in addition it can provide various types of image contrasts ( $T_1$ ,  $T_2$ , diffusion coefficient), by a simple alternation of the pulse imaging sequence. The highest microwave frequency that was employed in our recent work was  $\sim 17$  GHz (in pulsed mode), with a miniature  $\sim 2.4$  mm dielectric resonator and a miniature imaging coil set located around it.<sup>15</sup> This configuration enabled us to achieve, for solid paramagnetic samples, a spin sensitivity of  $\sim 10^7$  spins for 1 h of acquisition time and an image resolution slightly better than 1  $\mu\text{m}$  (using  $\sim 1$   $\mu\text{s}$  gradient pulses with a maximum strength of  $\sim 55$  T/m).<sup>15</sup>

In order to further improve the image resolution, one must greatly improve the spin sensitivity- or, in other words, the signal-to-noise-ratio (SNR) of the measurement, since there are fewer and fewer spins in each imaged voxel as its size is decreased. Furthermore, one must increase the amplitude of the pulsed gradient (which spatially encodes the sample), and if possible, make it shorter in order to enable the observation of samples with a shorter  $T_2$ . In Refs. 15 and 18, we provide some formulas for spin sensitivity and image resolution for pulsed ESR imaging. The former can be expressed by

$$\text{SNR}_{\text{pulse}}^{\text{one second}} \approx \frac{\sqrt{2\mu_0 M \omega_0 V_V}}{8\sqrt{V_c} \sqrt{k_B T (1/\pi T_2^*)}} \sqrt{\frac{Q_u}{\omega_0}} \sqrt{\frac{1}{T_1}}, \quad (1)$$

<sup>a)</sup>Present address: Schulich Faculty of Chemistry, Technion – Israel Institute of Technology, Haifa 32000, Israel, Tel.: +972-4-829-3679, Fax: +972-4-829-5948, Electronic mail: ab359@tx.technion.ac.il.

where  $M$  is the specific net magnetization of the sample (units of  $[\text{JT}^{-1} \text{m}^{-3}]$ ), as given by the Curie law,<sup>19</sup>  $\omega_0$  is the Larmor angular frequency,  $k_B$  is the Boltzmann constant,  $T$  is the temperature,  $\mu_0$  is the free space permeability, and  $Q_u$  is the unloaded quality factor of the resonator. The symbol  $V_c$  represents the resonator's effective volume,<sup>9,15,18,20</sup> which is equal to the volume of a small hypothetical sample  $V_v$  (for example,  $[1 \mu\text{m}]^3$ ) usually located at the point where the resonator's microwave magnetic field is maximal, divided by the filling factor<sup>21</sup> of this small sample.<sup>9</sup> Here we assumed an averaging with a repetition rate equal to  $1/T_1$  for SNR improvement and that the bandwidth of excitation is chosen to match the linewidth of the imaged paramagnetic species in the sample,  $\Delta f = 1/\pi T_2^*$ .

The image resolution for an imaging sequence employing pulsed field gradients for phase-encoding (see also Fig. 5 below) is given by<sup>4,22</sup>

$$\Delta x = \frac{1}{(\gamma/2\pi) \int_t G_x dt}, \quad (2)$$

where  $\gamma$  is the electron's gyromagnetic ratio and  $G_x$  is the time-dependant pulsed field gradient's magnitude (at maximum gradient strength).

As noted in our previous work,<sup>15</sup> there is a sharp dependence of the single-voxel SNR on the microwave frequency. This is evident from Eq. (1) in which there is an explicit dependence of  $\omega_0^{1/2}$  and additional implicit dependencies of  $\omega_0$  in  $M$  (due to the Curie law) and an  $\omega_0^{1.5}$  implicit dependence in  $1/\sqrt{V_c}$  (since  $V_c$  is proportional to the wavelength  $\lambda^3$ , which is  $\sim 1/\omega_0^3$ ), leading to an overall expected dependence of up to  $\sim \omega_0^3$  for the single-voxel SNR versus frequency. The image resolution can also greatly benefit from an increase in the microwave frequency, because the applied gradient,  $G_x$ , can be much larger if the gradient coils are made smaller. For example, both for Maxwell pair and Golay gradient coils, the gradient efficiency,  $\eta$ , expressed in T/m A, is related to their linear dimension,  $a$ , as  $\eta \sim 1/a^2$ .<sup>23</sup> This corresponds to an expected frequency dependence of  $\eta \sim \omega_0^2$ , since the linear dimensions of the imaging probe are inversely proportional to the frequency. Furthermore, smaller coils mean smaller inductance—leading to the possibility of applying shorter gradient pulses, which facilitate the imaging of spin probes with a short relaxation time  $T_2$ .

In view of the above, it is clear that there is a significant incentive to increase the magnetic field (i.e., the microwave frequency) of the ESR microimaging system in order to improve both sensitivity and image resolution. We have, therefore, taken the initiative of further advancing the field of ESR microscopy by developing a Q-band ( $\sim 35$  GHz) pulsed system. This system should enable, according to Eqs. (1) and (2), to improve sensitivity relative to the 17 GHz system by a factor of up to 8, and three-dimensional (3D) resolution by a factor of up to 2 or 4 (depending on whether we are SNR limited or gradient-strength limited, respectively). Here we present the various components and the detailed design of this new Q-band microimaging system that currently operates only around room temperature. Furthermore, we provide both theoretical and experimental data regarding the spin

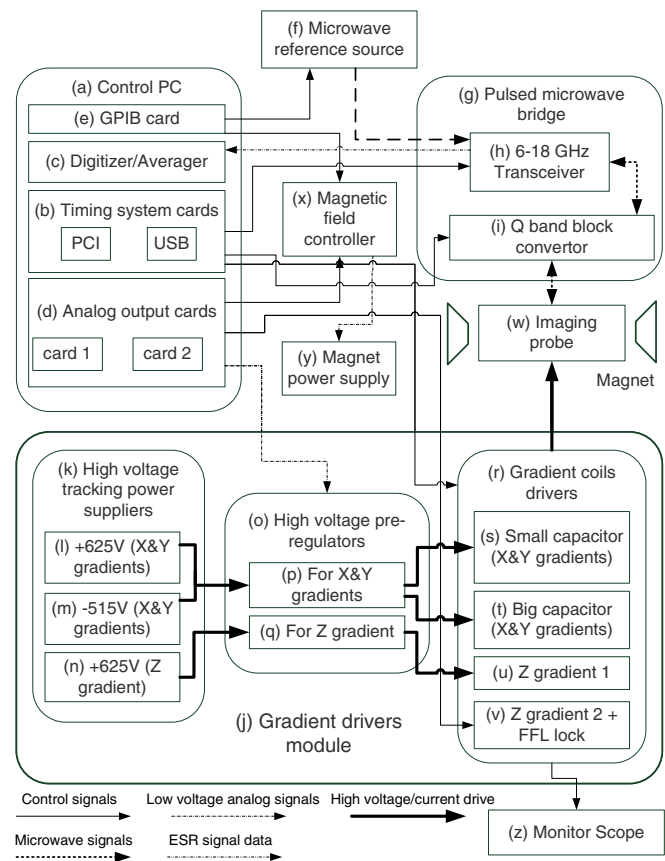


FIG. 1. Block diagram of the entire Q-band ESR microimaging system

sensitivity of the new Q-band probe, the strength of gradients, and the available imaging resolution.

## II. The Q-BAND ESR MICROIMAGING SYSTEM

Figure 1 presents an overall block diagram of the entire ESR microscopy system. It is based on both commercial and homemade main modules and submodules. The system is constructed from the following main modules: (a) personal computer (PC) which supervises the image acquisition process through LABVIEW (National Instruments), MATLAB (Mathworks) and C++ (Microsoft) software. The PC includes: (b) two timing cards—one is a PulseBlasterESR-Pro from SpinCore, which has 21 TTL outputs, time resolution of 2.5 ns and a minimum pulse length of 2.5 ns, and the other is PulseBlasterUSB, also from SpinCore, which has 24 TTL outputs with time resolution of 10 ns; (c) an 8 bit dual-channel PCI-format digitizer card for raw data acquisition and averaging, with a sampling rate of 500 MHz and averaging capability of up to 0.7 M waveforms/s (AP-235, Acqiris); (d) two PCI analog output cards, each having eight outputs with 16 bit resolution (PCI-6733, National Instruments); and (e) a general purpose interface bus (GPIB) control card (National Instruments). The microwave part of the system includes: (f) a microwave reference source (HP8672A) with a power output of 10 dBm in the 2–18 GHz range; (g) a homebuilt pulsed microwave bridge containing: (h) a 6–18 GHz low power transceiver and (i) a 33–36 GHz frequency block converter

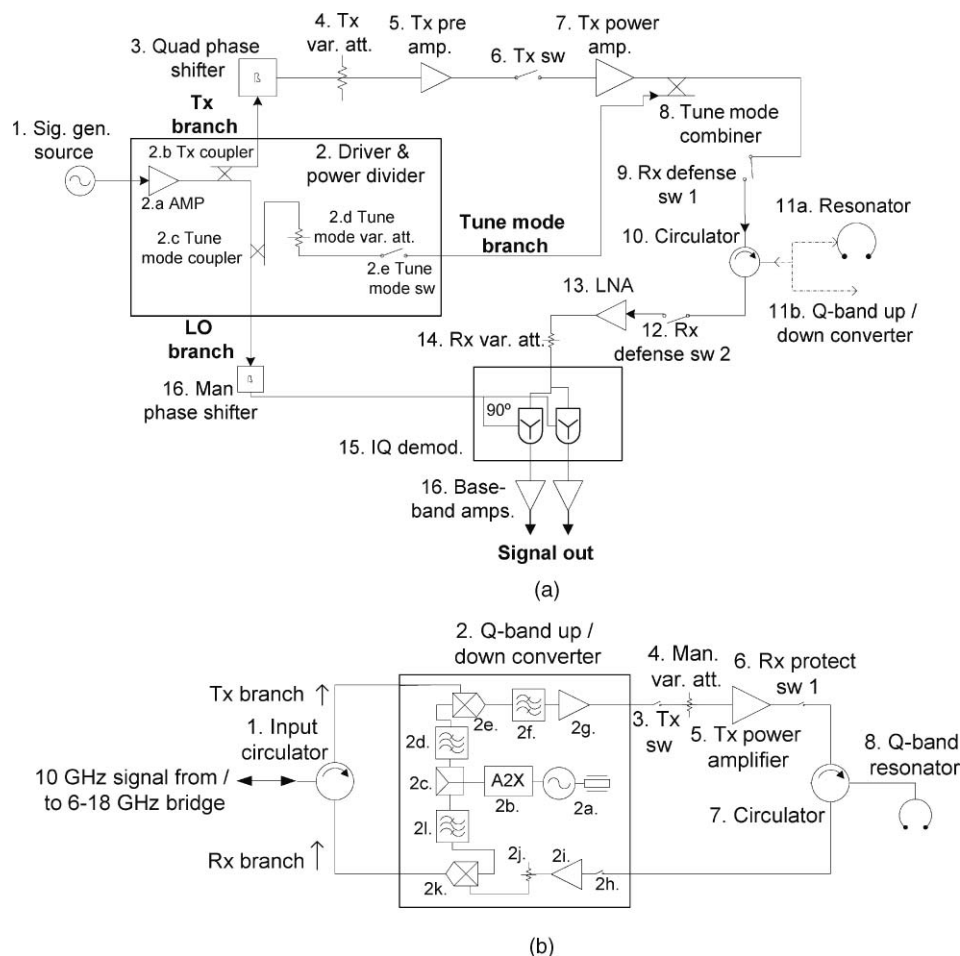


FIG. 2. Block diagram of the microwave bridge module. The bridge is comprised of a base-band unit (a) that operates in the 6–18 GHz range and an up-/down-converter unit (b).

(homebuilt). The gradient drivers' module (j) is a complex array of the following submodules. It contains (k) high-voltage power supplies (Lambda GEN600–2.6), each with a 1.6 kW output, with voltages of +625 and –515 V [supplies (l) and (m)] and another of +625 V [supply (n)]. In addition, there are two high-voltage preregulators (homemade), one that works up to a voltage of +625V/–515V, for the X and Y gradients (p) and the other, for the Z gradient (q), working up to +625 V. The outputs of these regulated supplies go to the gradient coils drivers' module (r). This module contains two pulsed drivers for the X and Y coils—one with small capacitors (s) for relatively short pulses and small currents, and one with large capacitors (t) for relatively long gradient pulses and high current. A similar pulsed drive is also provided for the Z gradient coil (u), but only with positive charge voltage. In addition, this module also contains a low-current/low-voltage drive to the Z coil for supplying the latter with a constant gradient and also for supplying the field-frequency lock coil with dc current drive (v). This enables locking the local field in the probe to the resonance field of the sample, regardless of possible external fields or frequency drifts in the system. (see below for explanations regarding possible gradient drives to the Z coil.) The microwave and gradient currents go directly to the homebuilt microimaging probe (w). Finally, we have a magnetic field controller (x) (Lakeshore model 475) that sta-

bilizes the magnetic field in the magnet (10in. variable gap from GMW) through the current drive in the magnet power supply (y) (Walker HS-75150–3SS). A monitor scope is embedded as part of the system to examine its variety of analog pulses and digital triggers (z).

We now provide more details regarding the homebuilt modules and submodules.

## A. Microwave bridge

Figure 2 provides a block diagram of the microwave bridge, while Tables I and II list its components. The 6–18 GHz transceiver [Fig. 2(a)] generates microwave pulses with timing and controlled phase as dictated by the computer software. When the system is operated at the 6–18 GHz range, the output of the transceiver goes directly to the resonator, marked as 11a in Fig. 2(a) In the present work, the pulses coming from this transceiver (which are commonly in the 8–11 GHz range during Q-band system operation) are up-converted by mixing them with a 25 GHz local source, up to the Q-band frequency range in the block converter submodule. Following the up-conversion, the microwave pulses are amplified and directed into the imaging probe (marked as item 8 in Fig. 2(b)—the Q-band resonator). The returning ESR signal from the probe is amplified by the block converter



TABLE I. Microwave components of the 6–18 GHz module in the microwave bridge.

Item number in Fig. 2(a)	Item description
1	Signal generator (HP 8672A)
2	Driver and power divider (homemade printed circuit)
2a	Amplifier (Agilent AMMP 5618)
2b	Tx directional coupler 10 dB
2c	Tune mode directional coupler 30 dB
2d.	Tune mode variable attenuator (Hittite HMC346)
2e	Tune mode switch (Hittite HMC 547)
3	Quadrature phase shifter (Miteq DPS-0618–360–9–5)
4	Tx variable attenuator (General Microwave D1958)
5	Tx preamplifier (Pasternack PE-1523)
6	Tx high-speed PIN diode switch (American Microwave Corporation SWN-AGRA -1DR-ECL-GAK0-LVT)
7	Tx power amplifier (Quinstar Technology QPJ-06183640-A0-)
8	Tune mode combiner (Narda 4246B-20)
9	Rx defense switch 1 (American Microwave SWG218 – 2DR-STD)
10	Circulator (Pasternack PE-8304)
11	Two possible connection options:
11a	Dielectric resonator
11b	Q-band up- / down-converter
12	Rx defense switch 2 (American Microwave SWG218–2DR-STD)
13	LNA amplifier (Phase1 SLL83020)
14	Rx variable attenuator (General Microwave D1958)
15	IQ demodulator (Marki IQ0618-LXP)
16	Baseband amplifiers (Analog Modules 322–6-50)

submodule and then converted back to the frequency range of 6–18 GHz (in practice, 8–11 GHz, corresponding to the 33–36 GHz range). These signals are then amplified and mixed with a reference source to provide a phase-sensitive ESR signal that can be further digitized by the computer. Another mode of action of the microwave system is called “tune-mode” in which a low-power CW is transmitted to the probe and the returned signal is monitored as a function of frequency to provide the reflection coefficient of the resonator as a function of frequency. This mode currently works only for the 6–18 GHz system and has not been implemented yet in the Q-band system.

## B. Gradient drivers' module

This module [marked as (j) in Fig. 1] includes nine submodules that facilitate the generation of a wide variety of gradient current drives, mainly including powerful short-gradient pulses. The X and Y gradients' drive is produced by five of these submodules. They include two high-voltage/high-power

TABLE II. Microwave components of the Q-band up-/down-converter module in the microwave bridge.

Item number in Fig. 2(b)	Item description
1	Circulator (Pasternack PE-8304)
2	Q-band up- / down-converter (Spacek Labs TR35–10PLO):
2a	12.5 GHz crystal (100 MHz) stabilized PLO
2b	25 GHz $\times$ 2 multiplier
2c	WR28 power divider
2d	LO low pass filter
2e	Up-converter mixer
2f	RF bandpass filter
2g	Tx amplifier (34 dB gain, +24 dBm)
2h	PIN switch Rx protect
2i	LNA (45 Db gain, 2.5 dB NF)
2j	Variable Rx gain attenuator
2k	Down converter mixer
2l	LO low pass filter
3	Tx pin switch (Millitech PSH28)
4	Tx manual variable attenuator (Dorado VA28)
5	Tx power amplifier (Quinstar QPN-34033640130)
6	Rx protect pin switch 1 (Hughes 47971H + Millitech PSH28)
7	Wr28 circulator (Hughes 45161H)
8	Q-band resonator

dc power supplies that are set to +625 V and –515 V. These power supplies feed the preregulated power supplies that provide variable voltage based on an analog input from the computer. The basic schematics for one of these preregulated supplies (there is one for X and the other for Y, both located in the same submodule enclosures), is shown in Fig. 3(a) They can supply currents of up to 10 A and their voltage can change from 0 to 6250 V (or –515 V) in a few microseconds (according to the input voltage from the computer). The outputs of these preregulated power supplies serve as input for the half-sine coil drivers. We have two types of half-sine submodule drivers in our system. One is for producing relatively short pulses with relatively small currents (from 150 ns and 9 A, up to 500 ns and 33 A, when connected to a nominal 0.6  $\Omega$  2.75  $\mu$ H coil) and the other is for producing relatively long gradient pulses and high peak currents (750 ns and 50 A, up to 1400 ns and 94 A). These half-sine drivers are based on the principle of charging a capacitor and then discharging it into the gradient coil, as described by Conradi and co-workers.<sup>24</sup> A recent publication by our group provides more details about this new version of the pulsed driver, including detailed results of electrical tests that were made with it.<sup>25</sup> As for the drivers of the Z coil, there are three different possibilities for it, facilitating the use of the imaging sequences, as described in Fig. 5 The first option is to use another 625 V power supply to control a preregulated power supply, similar to the one described in Fig. 3(a) but with a positive output only. This voltage can, again, be used to feed a separate half-sine driver dedicated to the Z coil that has similar capabilities to the one mentioned above, but with just half the current (due to the

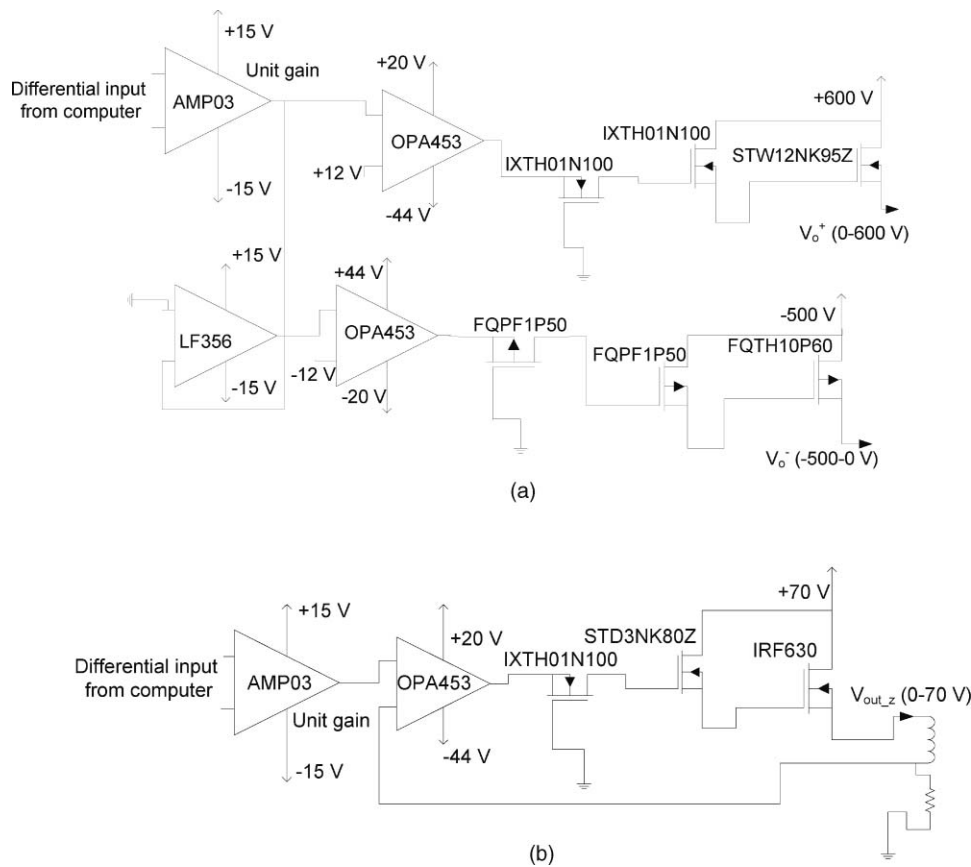


FIG. 3. (a) Basic schematic of the preregulated supplies used as part of the gradient drivers' module. These are bipolar units that receive a differential analog input from the computer in the range of  $\pm 8$  V and amplify it by a factor of  $\sim 80$ . (b) Basic schematic of the rectangular current pulse driver. This unit also receives a differential analog input from the computer, which determines the amplitude of the current into the gradient coil (up to 10 A).

positive-only supply it receives). A second option is to put a constant current drive into the Z coil. This is executed by another submodule using the electronic circuit described in Fig. 5 of Ref. 16. Such a constant drive can produce up to 3 A of current. A third option is to use a fast rectangular current pulse driver that can deliver up to 10 A of current into the Z coil, for a duration of  $\sim 2$ – $10$   $\mu\text{s}$  with typical rise and fall times of  $\sim 1$   $\mu\text{s}$ . This greatly reduces the average power dissipation in the gradient coils and, thus, enables one to increase significantly the gradient magnitude. The schematic diagram of this rectangular current pulse driver is shown in Fig. 3(b)

### C. Microimaging probe

The overall structure of the microimaging probe is shown in Fig. 4. The heart of this probe is a miniature microwave dielectric ring resonator [Fig. 4(b)]. It is made of a rutile ( $\text{TiO}_2$ ) single crystal (MTI corporation, CA, USA) machined to a diameter of 1.3 mm and a height of 0.22 mm, with center hole diameter of 0.6 mm. The resonator is fed by a loop at the end of a coaxial semirigid line (o.d. 0.85 mm) as shown in Fig. 4(b). The resonator is excited to its  $\text{TE}_{01\delta}$  resonance mode<sup>26</sup> with the microwave magnetic field distribution of this resonance mode shown in Fig. 4(c). The semirigid line is connected to the microwave bridge by a standard WR-28 waveguide through a waveguide-to-coax adapter. The relative

position of the coaxial line with respect to the resonator ring can be adjusted by manual XY stages (MDE261-NM and MDE265-NM from Elliot Scientific, UK). The resonance frequency of the resonator was found to be 33.84 GHz and its loaded  $Q$ -factor (measured by a microwave vector network analyzer—Agilent E8361A) was  $Q_L = 455$  ( $= Q_u/2$  at critical coupling) when it was placed in a cylindrical brass shield with 2.8 mm i.d. This  $Q$  value is for an empty resonator and it does not change much when a nonlossy sample is inserted to it. When the brass shield is replaced by a thin, 1  $\mu\text{m}$  gold gradient-coil shield [see Fig. 4(d)], the  $Q_L$  value drops to  $\sim 170$ , probably due to some radiation losses. The field distribution shown in Fig. 4(c) is for 1 W of input power and thus can be used to calculate the conversion factor from microwave power to magnetic field, which is found to be  $C_p = 21$   $\text{G}/\sqrt{\text{W}}$  (in the center of the resonator). The measured value was found to be  $\sim 8$   $\text{G}/\sqrt{\text{W}}$ , based on the optimization of the signal after a  $\pi/2$  pulse of 30 ns while measuring the incident power at the output of the bridge. The reasons for the relatively low measured value (compared to the calculation) are probably losses and impedance mismatches from the bridge output to the resonator, as well as an actual  $Q$  value lower than the calculated one. The resonator's effective volume,  $V_c$  (see above), is calculated to be  $\sim 0.51$   $\text{mm}^3$ , also based on the field distribution as shown in Fig. 4(c).

Surrounding the resonator [Fig. 4(d)] there is a cylindrical shield with an i.d. of 2.5 and an o.d. of 2.8 mm, made of

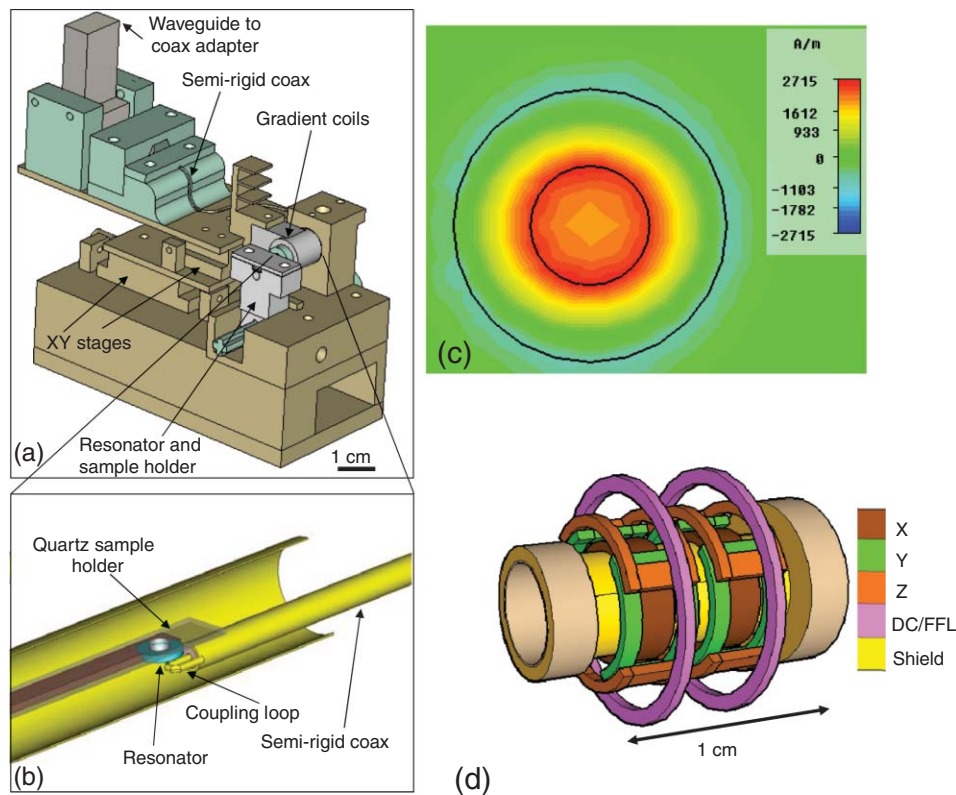


FIG. 4. (Color) (a) Schematic drawing of the imaging probe. (b) Enlarged image of the area in the probe where the sample is positioned, inside the resonator and at the center of the gradient-coil structure [this structure is removed from drawing (b) for clarity]. (c) Microwave magnetic field spatial distribution in the XY plane of the resonator. (d) Schematic drawing of the gradient-coil structure in the microimaging probe that surrounds the resonator. It should be noted that the x axis of the gradient coils (along the cylinder axis) is parallel to the direction of the laboratory-frame static magnetic field.

rexolite plastic covered by a thin gold layer with a thickness of  $1 \mu\text{m}$ . The gradient coils' structure is positioned around this shield, as shown in Fig. 4(d). The gradient coils include a set of X-, Y-, and Z-gradient coils. The structure of the X-gradient coil is a simple Maxwell pair, the coils of the pair are connected in parallel and have a total inductance of  $0.75 \mu\text{H}$ , resistance of  $0.55 \Omega$ , and a magnetic gradient efficiency of  $4.66 \text{ T/m} \cdot \text{A}$ . It is positioned at a distance of  $1.4 \text{ mm}$  from the axis of the cylinder (the coil radius). The Y-gradient coil is based on Golay's geometry and has a total inductance of  $1.7 \mu\text{H}$ , resistance of  $0.55 \Omega$ , and an efficiency of  $2.7 \text{ T/m} \cdot \text{A}$ . It is positioned at a distance of  $1.8 \text{ mm}$  from the cylinder's axis. Both the X- and Y-gradient coils are driven by the pulse half-sine current drivers described above. The Z-gradient coil is also based on Golay's geometry, with a possibility to connect its two coil pairs in series or in parallel. When connected in series, their total inductance is  $7 \mu\text{H}$  and their resistance is  $2.2 \Omega$ , making it more suitable for a static gradient rather than a pulsed operation. The gradient efficiency of the coils for the serial connection is  $3.5 \text{ T/m} \cdot \text{A}$ . When we employ phase gradients for the z axis (see Fig. 5 for available imaging pulse sequences), the Z coils are connected in parallel and have an inductance of  $1.75 \mu\text{H}$ , resistance of  $0.55 \Omega$ , and efficiency of  $1.75 \text{ T/m} \cdot \text{A}$ . They are positioned at a distance of  $2.4 \text{ mm}$  from the axis of the cylinder.

The imaging probe can accommodate flat samples that can be placed on the resonator [see Fig. 4(b)] or positioned directly inside the resonator (if they are small enough) for increased sensitivity. In case the sample needs to be sealed

(i.e., aqueous sample and/or deoxygenated sample), one can employ specially-prepared cuplike glass sample holders.<sup>27</sup> An example for such kind of sample will be provided in the experimental results below.

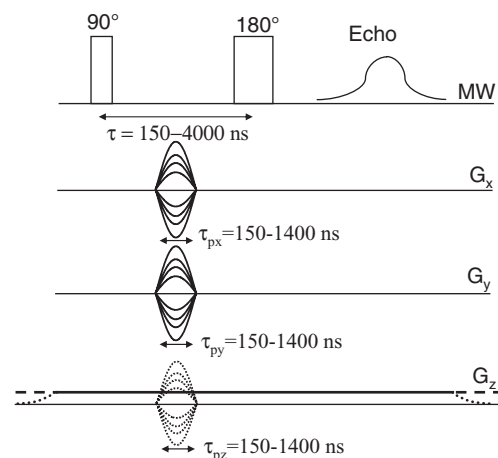


FIG. 5. Description of the possible imaging sequences supported by the hardware and software of the Q-band microimaging system. The microwave (MW) sequence is a simple Hahn echo. The spatial encoding for the x and y axes is achieved by phase gradients. The z axis can be either frequency-encoded via a constant or a rectangular-shaped gradient pulse, or via much stronger but shorter phase gradients (see text). It should be noted that the notation in this work is that the x axis of the gradient coils (along the gradient structure cylinder axis) is parallel to the laboratory-frame static magnetic field direction.

## D. Software and supported imaging sequences

The ESR imaging system is controlled via a PC that runs LABVIEW software, providing a convenient user interface. The software enables the user to define all relevant imaging pulse sequence parameters, such as: type of sequence (see Fig. 5); duration and position of microwave (MW) pulses; repetition rate of the sequence; gradient amplitudes' positions and duration; and the use of scripts to sequentially run several imaging sequences in an automated manner (for example, acquiring several images with varying  $\tau$ , which allows the later extraction of a spatially-resolved  $T_2$  image<sup>10</sup>). Underneath the LABVIEW interface, the software executes a variety of sub-programs written in C++ and MATLAB that directly control the signal generation and acquisition cards in the PC (see Fig. 1) and perform a variety of data postprocessing tasks that enable the display of the ESR images in real time, even on the basis of partially-acquired data.

## III. THEORETICAL SYSTEM PERFORMANCE

Here we shall present the theoretical prediction of the available resolution in the new Q-band ESR microimaging system. In general, the resolution of an ESR microimaging system is determined both by its absolute spin sensitivity (corresponding to the smallest number of spins that can be measured in each voxel) and the strength of the gradients' spatial encoding.<sup>9,15,20</sup> Spin sensitivity is more often the fundamental limitation of the system, especially for samples having a low spin concentration. Still, as sensitivity is increased, the capability of the magnetic field gradients must follow closely to facilitate the acquisition of high-resolution images for samples having relatively long or short relaxation times.

### A. Spin sensitivity

Following Eq. (1), the resonator's absolute spin sensitivity in spins per  $\sqrt{\text{Hz}}$  can be calculated via the expression<sup>18</sup>

$$\text{Sensitivity}_{\sqrt{\text{Hz}}}^{\text{spins}} \approx \frac{8\sqrt{V_c}\sqrt{k_B T(1/\pi T_2^*)}}{\mu_B \omega_0 \sqrt{2\mu_0}} \sqrt{\frac{\omega_0}{Q_u}} \sqrt{T_1} B_F, \quad (3)$$

where  $B_F$  is the Boltzmann population factor  $B_F = (1 + e^{-\frac{\hbar\omega_0}{k_B T}})/(1 - e^{-\frac{\hbar\omega_0}{k_B T}})$ , and  $\mu_B$  is the Bohr's magneton. Equation (3) assumes that the noise is four times larger than the theoretical lower limit (for a dominant Johnson noise source). Based on the resonator characteristics, as presented above, one can calculate the spin sensitivity to be  $\sim 1.5 \times 10^7$  spins/ $\sqrt{\text{Hz}}$  for a typical sample of LiPc crystals having  $T_1 = 3.5 \mu\text{s}$  and  $T_2 = 2.5 \mu\text{s}$  (assumed here to be equal to  $T_2^*$ ), at room temperature.

### B. Resolution

The theoretical image resolution (assuming SNR is not the fundamental resolution limit) in phase gradient imaging, such as in the imaging sequence shown in Fig. 5 for the x and y axes, was given in Eq. (2) above. Based on the characteristics of the gradient drivers' system and the efficiency

of the gradient coils, as described above, one can obtain from Eq. (2) the available resolution in our present Q-band system. For example, at the limit of the shortest gradient pulse of 150 ns, as noted above, we can provide a maximum current drive of 9 A into a nominal  $0.6 \Omega$   $2.75 \mu\text{H}$  gradient coil. This information can be used to obtain the available maximum gradient and resolution for this short pulse in the following manner.

The maximum current going into a gradient coil with inductance  $L$  and resistance  $R$ , via the discharge of a capacitor  $C$ , can be calculated from energy conservation arguments by the equation

$$\frac{CV_{\max}}{2} \approx \frac{LI_{\max}^2}{2} + \frac{I_{\max}^2 R}{2} T_{\text{pulse}}, \quad (4)$$

where  $T_{\text{pulse}}$ , is the half-sine pulse duration, given by  $T_{\text{pulse}} = \pi\sqrt{LC}$ . This leads to the expression

$$I_{\max} \approx \sqrt{\frac{C}{L + \pi R\sqrt{LC}}}. \quad (5)$$

In our gradient coils and driver system, most often  $L \gg \pi R\sqrt{LC}$  and thus the maximum current scales as  $1/\sqrt{L}$ . If we consider now, for example, the x axis gradient coil that has an inductance of  $0.75 \mu\text{H}$ , we can use Eq. (5) and the data above to calculate the available resolution in this axis. The coil is connected via a transmission line that has a self-inductance of  $\sim 1 \mu\text{H}$ , which leads to an overall inductance of  $\sim 1.75 \mu\text{H}$  as "seen" by the discharging capacitor. Now, as mentioned above, since for the short 150 ns gradient pulse a current of 9 A goes into a reference  $2.75 \mu\text{H}$  coil, it means that the maximum current in the x axis coil would be  $\sim 9\sqrt{(2.75/1.75)} = 11.3$  A, and  $T_{\text{pulse}} = 150\sqrt{(1.75/2.75)} = 120$  ns. The gradient efficiency of the x axis coil is  $4.66 \text{ T/m} \cdot \text{A}$ , meaning that the peak gradient is  $G_{\max} = 11.3 \cdot 4.66 = 52.6 \text{ T/m}$ . Based on  $T_{\text{pulse}}$  and  $G_{\max}$ , the resolution in this case can be calculated via Eq. (2) to be

$$\Delta x = \frac{1}{(\gamma/2\pi) \times 0.63 \times G_{\max} T_{\text{pulse}}} \approx 9 \mu\text{m}. \quad (6)$$

The same type of calculations can be done for the longest 1400 ns gradient pulses the system supports (in conjunction with a nominal  $2.75 \mu\text{H}$  coil). There, a peak current of  $\sim 117$  A is expected for the x axis gradient coil, corresponding to a maximum gradient of  $\sim 545 \text{ T/m}$ , applied during a half-sine pulse of  $\sim 1170$  ns. This data, based on Eq. (2) gives us the maximum available theoretical resolution of the present ESR microimaging (ESRM) system, which is  $\sim 88$  nm.

In practice, as noted above, in most cases the resolution is limited by the spin sensitivity. Thus, even for a high spin-concentration sample of LiPc, having  $\sim 10^8$  spins per  $[1 \mu\text{m}]^3$ , the number of spins in  $[100 \text{ nm}]^3$  would be  $\sim 10^5$ . This is more or less the theoretical sensitivity limit of our current system, given a reasonable maximum measurement time of 24 h (leading to a spin sensitivity of  $\sim 6 \times 10^4$  spins with SNR of 1). This implies that the available gradient capability of the current system should be enough for all relevant micron- and nanoscale imaging experiments, carried out with the present ESRM setup sensitivity at room temperature.



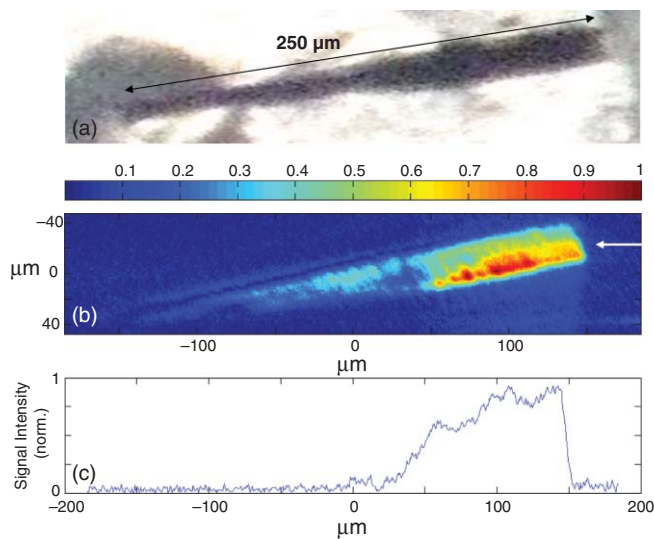


FIG. 6. (Color) Optical (a) and 2D ESR image (b) of a single LiPc crystal. The crystal was positioned with its long axis in the XY plane of the ESR image. (c) A cross sectional cut along the x axis of the 2D image in a position marked by the white arrow, showing the intensity changes when going from the crystal signal to the noise level.

#### IV. EXPERIMENTAL RESULTS

Figure 6 provides typical experimental results for the two-dimensional (2D) imaging of a solid LiPc crystal sample. The sample was flushed with helium gas during the measurement to eliminate the presence of oxygen, which greatly reduces its relaxation times. Here we employed the imaging sequence shown in Fig. 5 but only with X- and Y-phase gradients with  $\tau = 800$  ns, and the gradient pulses lengths were  $\sim 700$  and  $\sim 800$  ns for X and Y, respectively. The number of pixels in the image is  $1800 \times 260$  (we show just part of the image where the crystal is located) and measurement time was 2.5 h with a sequence repetition rate of 6 kHz (limited by heat dissipation in the gradient coils). By comparing the optical image [Fig. 6(a)] to the ESR image [Fig. 6(b)] and counting the number of pixels along the sample one can provide the theoretical pixel resolution, which is 440 and 650 nm for the x and y axes, respectively. Similar values can also be asserted from measurements of the time integral of the current going into the gradient coils, which after multiplication by the gradient coils' efficiency can be plugged in Eq. (2) to provide the image resolution. In this experiment, the maximum gradient current-time integral was measured to be  $1.86 \times 10^{-5}$  and  $2.04 \times 10^{-5}$  A s for the X and Y gradients, respectively. This provides a resolution of  $\sim 412 \times 642$  nm (using the calculated gradient efficiency values of 4.66 and 2.7 T/m · A, as described above, for the x and y axes, respectively). Another possible measure of the resolution is to look at an area in the image where the signal should drop to zero very fast (where the sample has a sharp boundary) and compare it with the experimental image's "fall-down" rate. Figure 6(c) shows such a result for a cross section of the 2D image taken along a line whose position is marked by the arrow in Fig. 6(b). Here it takes  $\sim 14$  resolution points for the signal to drop from its maximum to the noise level, which corresponds to  $\sim 5.8 \mu\text{m}$  in resolution. However, one should

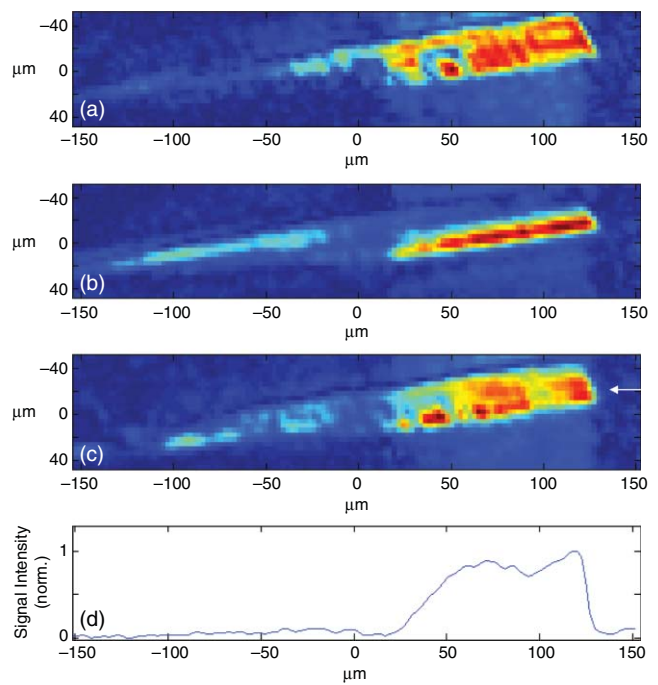


FIG. 7. (Color) (a)–(c) Two-dimensional cuts taken from the complete 3D image of the same LiPc shown in Fig. 6 (d) A cross sectional cut along the x axis of the 2D image in a position marked by the white arrow, showing the intensity changes when going from the crystal to the noise level.

note that, in this case, the crystal height in the Z dimension is  $\sim 25 \mu\text{m}$  (see below) and there is an unavoidable tilt in its vertical positioning. As a result of that, the signal is "spread out" in the *projected* 2D image that we obtain, and it is clear that in this case such test will provide a much higher value than the actual resolution. (A similar test on a 2D slice taken from a 3D image, which gives much more reasonable results, will be described below). The 1D cross section of the signal also shows the good signal of the measurement, which is a factor of  $\sim 50$  above the rms of the noise (sampled at areas of the image where no signal is present). Assuming a voxel size of  $0.44 \times 0.650 \times 25 \mu\text{m}$  and based on the estimated number of  $\sim 10^8$  spins in  $1 \mu\text{m}^3$  of LiPc,<sup>28</sup> one obtains the number of spins in each voxel to be  $7.15 \times 10^8$  spins. This gives a spin sensitivity of  $\sim 1.4 \times 10^7$  spins for the SNR we obtained in the imaging time employed for this image.

Figure 7 shows the 3D imaging results of the same LiPc crystal that appears in Fig. 6. The spatial encoding along the z axis was achieved by adding a third phase-gradient pulse along this axis (the half-sine pulses illustrated by the dashed line in the bottom of Fig. 5). The number of pixels in the image is  $256 \times 50 \times 20$ , the measurement time is 25 min (repetition rate of 10 kHz), and the theoretical pixel resolution, based on the crystal size in the x and y axes, is  $\sim 2.2 \times 3.25 \mu\text{m}$ , while for the z axis the resolution is  $\sim 3.5 \mu\text{m}$ , based on images taken with a similar gradient on a crystal with vertical orientation (see the results of Fig. 8 below). Here, the same cross section resolution test is also applied [Fig. 7(d)], and the signal drops down in just one pixel—corresponding well to the  $2.2 \mu\text{m}$  x-axis resolution [by taking a thin 2D slice out of a 3D image one avoids the projection problem mentioned above in the context of Fig. 6(c)].

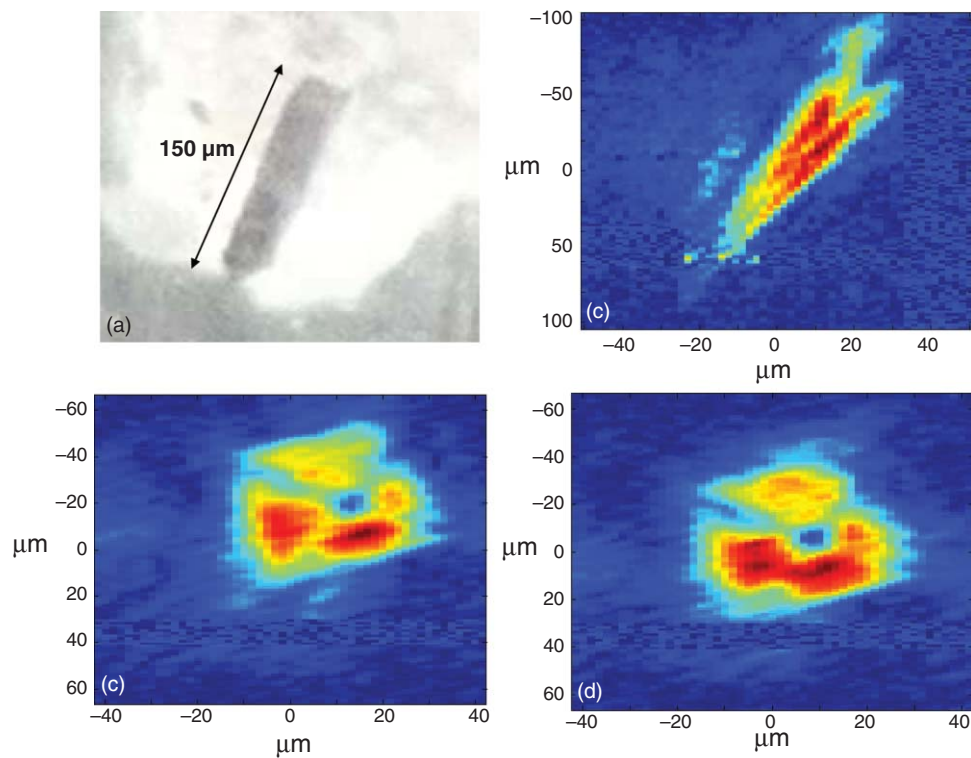


FIG. 8. (Color) Optical (a) and ESR images (c)–(d) of another LiPc crystal that was placed with its long dimension in the XZ plane. The 2D ESR images are taken in the XZ (b) and XY (c)–(d) planes, based on the 3D information obtained during image acquisition.

The spin sensitivity here is  $\sim 5.8 \times 10^7$  spins, based on the SNR we obtained in the imaging time employed for this image (much shorter than that of Fig. 6).

The last example of high-resolution solid-sample imaging is given in Fig. 8, for another LiPc crystal that was placed

in a more vertical position inside the resonator. A 3D image with  $160 \times 100 \times 170$  voxels was acquired at a repetition rate of 10 kHz over slightly less than 5 h of acquisition time. Here the theoretical resolution (based on the number of voxels and crystal size, as seen in the optical microscopy image) is

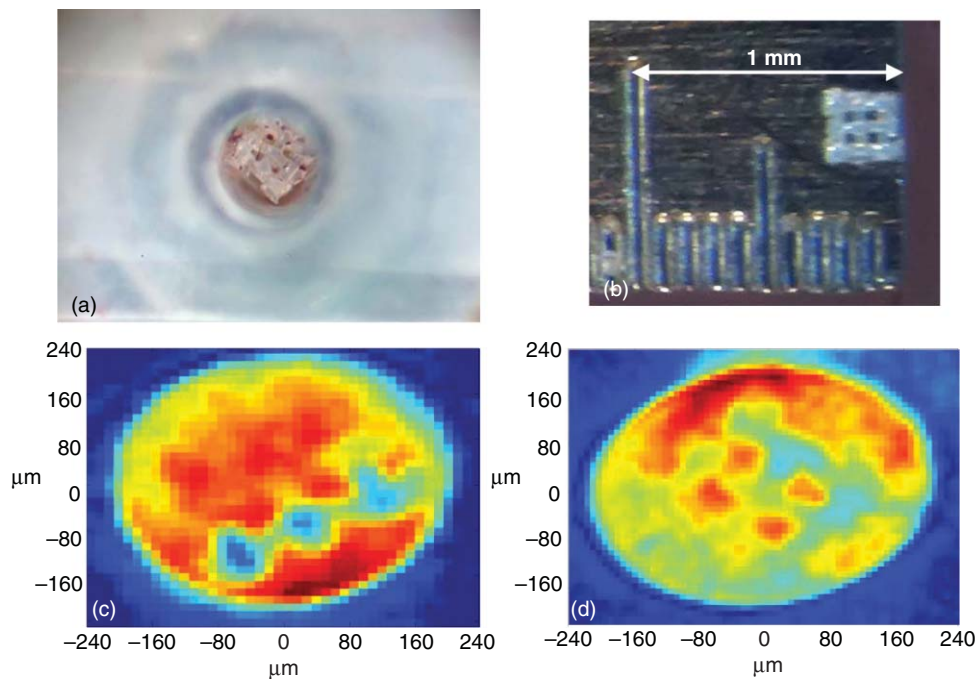


FIG. 9. (Color) (a) Optical image of a thin nylon mesh in the rexolite sample holder. (b) Another look at the mesh outside the holder. (c) Two-dimensional cut taken from a 3D ESR image of the mesh in trityl solution, where the mesh was placed vertically in the sample holder. (d) The same as (c), but for a mesh placed horizontally (in the XY plane) of the sample holder and imaging probe.

$\sim 1.1 \times 1.62 \times 1.75 \mu\text{m}$ . The spin sensitivity for this acquisition time is  $\sim 7 \times 10^6$  spins.

Solid LiPc crystals have a relatively high spin concentration and do not degrade the quality factor of the resonator. However, many of the potential applications of the ESRM system presented here involve the measurement of biological samples that are in aqueous media using exogenously administered paramagnetic species with a relatively low spin concentration.<sup>9,10</sup> For this reason, we also tested the system with special test samples composed of water solutions of a stable free radical. To avoid dehydration in these types of samples we reverted to the use of a slightly larger imaging probe than the one presented above, which has a double-stacked resonator rather than a single resonator.<sup>12,29</sup> Each individual resonator ring in this double-stacked structure is made of rutile with 1.14 mm o.d, 0.56 mm i.d, and a height of 0.22 mm. Rings separation is 0.3 mm. This enables us to use a larger sample volume with potentially long (up to  $\sim 1$  mm) samples. Figure 9 shows the results of such measurements for two different samples made of 1 mM liquid solution of deuterated Finland trityl radical<sup>3</sup> in normal aerobic conditions, each containing a thin woven nylon mesh embedded in it. The nylon mesh has apertures of  $50 \times 50 \mu\text{m}$  and a wire diameter of  $39 \mu\text{m}$ . The sample is held by a cuplike sample holder made of rexolite with an i.d of 0.4 mm and an o.d of 0.55 mm that fits into the resonator.<sup>10</sup> Upon insertion into the resonator, the loaded  $Q$  value dropped to  $\sim 50$ . In the sample depicted in Fig. 9(c) the mesh was placed almost vertically and the 2D cut clearly shows the mesh wires in the trityl solution. The mesh in Fig. 9(d) was placed horizontally on some pieces of filter paper (in order to position it in the center of the double-stacked resonators structure). The signal from the four mesh voids is visible in the center but there is also some signal interference due to the presence of the filter paper near the mesh, limiting the presence of trityl solution. The 3D images from which these 2D cuts were taken have  $128 \times 64 \times 32$  and  $220 \times 100 \times 32$  voxels for Figs. 9(c) and 9(d), respectively. A full 3D phase encoding image acquisition scheme was employed for both samples. The interpulse separation values,  $\tau$ , were 300 and 360 ns with acquisition times of 75 min and 5 h, respectively. The repetition rate was 30 kHz for both samples, while the resolutions of the measurements are  $\sim 10.5 \times 11.7 \times 40$  and  $\sim 6.8 \times 7.7 \times 40 \mu\text{m}$  which, based on the spin concentration and the image SNR, lead to a spin sensitivity of  $\sim 8 \times 10^7$  and  $3 \times 10^7$ , respectively.

## V. DISCUSSION

The new Q-band ESRM system presented here significantly improves upon the resolution achieved in previous experiments and constitutes, to the best of our knowledge, the state-of-the-art in induction-detection-based ESR imaging. In the case of solid samples with a high spin concentration, we obtained here for pure 2D imaging a resolution as good as  $\sim 440$  nm, compared to  $\sim 950$  nm in previous work carried out at 17 GHz.<sup>15</sup> In 3D imaging, we managed to obtain voxels with a similar resolution of  $\sim 1.5 \mu\text{m}$  in all three axes, providing an overall voxel volume of  $\sim 3.1 [\mu\text{m}]^3$ . This can be compared to the smallest voxel volume of  $\sim 13 [\mu\text{m}]^3$  achieved

in previous work at 17 GHz,<sup>15</sup> where the  $z$  axis resolution was much inferior to that of the  $x$  and  $y$ . In the case of liquid samples with a low spin concentration, we showed 3D image resolution results that are similar to those shown at 17 GHz,<sup>12</sup> but with a fully aerobic rather than a deoxygenated trityl solution. This means that the  $T_2$  values we had to deal with in the present measurements are in the order of 500 ns, compared to several microseconds in the previous work. This makes the pulsed imaging work much more challenging; however, aerobic conditions are without doubt much more relevant for many biological samples.<sup>10</sup> The small size of the imaging probe with its efficient gradient coils and the powerful new gradient drivers were cardinal in achieving such imaging capability for species with a relatively short  $T_2$ .

Another important incentive to move to a higher frequency is the expected improvement in spin sensitivity. Based on Eq. (3) and the resonator properties presented above, one can expect an improvement by a factor of  $\sim 2.8$  in spin sensitivity, when going from the 17 GHz resonator (with an effective volume  $V_c$  of  $1.34 \text{ mm}^3$  and  $Q_u = 1000$ <sup>15</sup>) to the one at Q-band ( $V_c = 0.51 \text{ mm}^3$  and  $Q_u = 170$ ). In practice, the improvement we saw was approximately by a factor of 2 ( $\sim 7 \times 10^6$  compared to  $\sim 1.3 \times 10^7$  at 17 GHz<sup>12,15</sup>) when a similar number of averages were employed during image acquisition. This relative change in sensitivity is very close to the theoretical expectation (keeping in mind that we did not consider in detail the transmission line losses and also preamplifier and protection switches performances). It should be noted, however, that while we managed to get a modest SNR improvement, a certain gap still exists between the expectations of Eq. (3) (predicting  $\sim 1.5 \times 10^7$  spins/ $\sqrt{\text{Hz}}$  for optimal resonator  $Q_u = 910$  with brass shield and LiPc sample) and the sensitivity we obtained in this work ( $\sim 1.6 \times 10^8$  spins/ $\sqrt{\text{Hz}}$ , but with the thin gold shield having  $Q_u = 340$ ). The reduction in  $Q$  explains part of this gap, but we believe that there is more to improve in that respect, especially with regards to transmission line losses and resonator coupling issues, and certainly also to try and regain the lost parts in  $Q$  by improving the gradient coils' shield geometry.

It can, therefore, be concluded that the main advantage of migrating to a Q-band frequency range ( $\sim 35$  GHz) is the possibility to apply much more powerful gradients with shorter duration times, which opens up the possibility to measure at high-resolution spins with relatively short relaxations times. The availability of powerful gradients also facilitates the imaging at very high resolution of solid samples with high spin concentrations. The SNR improvement, although currently rather small, is also of importance for all types of samples. Other important new features of the system include the higher voltage drive of the gradient drivers, the possibility to apply phase gradient encoding in all three imaging axes, and the flexible and advanced control software. These entireties of modules and features constitute a complete system, which is ready to address a variety of applications in physics, materials science, and biology.<sup>9,10,12,15</sup> An extension of the work to higher frequencies may further improve sensitivity and resolution. However, as we argued before in a detailed analysis,<sup>5,20</sup> with the type of dielectric resonators we employ, it is hard to foresee further improvements beyond  $\sim 60$  GHz

(mainly due increased transmission line losses, deterioration of microwave preamplifier performances, and increased resonator and sample losses—especially for liquid samples).

## ACKNOWLEDGMENTS

This work was partially supported by Grant No. 213/09 from the Israeli Science Foundation, Grant No. 2009401 from the United States-Israel Binational Science Foundation, Grant No. 201665 from the European Research Council (ERC), and by the Russell Berrie Nanotechnology Institute at the Technion.

- <sup>1</sup>S. Som, L. C. Potter, R. Ahmad, and P. Kuppasamy *J. Magn. Reson.* **186**, 1 (2007).
- <sup>2</sup>A. Blank, Y. Talmon, M. Shklyar, L. Shtirberg, and W. Harneit *Chem. Phys. Lett.* **465**, 147 (2008).
- <sup>3</sup>Y. Talmon, L. Shtirberg, W. Harneit, O. Y. Rogozhnikova, V. Tormyshev, and A. Blank *Phys. Chem. Chem. Phys.* **12**, 5998 (2010).
- <sup>4</sup>P. T. Callaghan, *Principles of Nuclear Magnetic Resonance Microscopy* (Oxford University Press, Oxford, UK, 1991).
- <sup>5</sup>*Multifrequency Electron Paramagnetic Resonance, Theory and Applications*, edited by S. K. Misra (Wiley-VCH, Berlin, 2011).
- <sup>6</sup>P. Kuppasamy, M. Chzhan, K. Vij, M. Shteynbuk, D. J. Lefer, E. Giannella, and J. L. Zweier *Proc. Natl. Acad. Sci. U. S. A.* **91**, 3388 (1994).
- <sup>7</sup>G. L. He, A. Samouilov, P. Kuppasamy, and J. L. Zweier, *Mol. Cell. Biochem.* **234**, 359 (2002).
- <sup>8</sup>K. I. Yamada, R. Murugesan, N. Devasahayam, J. A. Cook, J. B. Mitchell, S. Subramanian, and M. C. Krishna, *J. Magn. Reson.* **154**, 287 (2002).
- <sup>9</sup>A. Blank, C. R. Dunnam, P. P. Borbat, and J. H. Freed, *J. Magn. Reson.* **165**, 116 (2003).
- <sup>10</sup>R. Halevy, V. Tormyshev, and A. Blank, *Biophys. J.* **99**, 971 (2010).
- <sup>11</sup>E. Suhovoy, V. Mishra, M. Shklyar, L. Shtirberg, and A. Blank *EPL* **90**, 26009 (2010).
- <sup>12</sup>A. Blank, J. H. Freed, N. P. Kumar, and C. H. Wang, *J. Controlled Release* **111**, 174 (2006).
- <sup>13</sup>W. Harneit, C. Meyer, A. Weidinger, D. Suter, and J. Twamley, *Physica Status Solidi B* **233**, 453 (2002).
- <sup>14</sup>A. Blank, C. R. Dunnam, P. P. Borbat, and J. H. Freed, *Appl. Phys. Lett.* **85**, 5430 (2004).
- <sup>15</sup>A. Blank, E. Suhovoy, R. Halevy, L. Shtirberg, and W. Harneit, *Phys. Chem. Chem. Phys.* **11**, 6689 (2009).
- <sup>16</sup>A. Blank, C. R. Dunnam, P. P. Borbat, and J. H. Freed, *Rev. Sci. Instrum.* **75**, 3050 (2004).
- <sup>17</sup>A. Blank, R. Halevy, M. Shklyar, L. Shtirberg, and P. Kuppasamy, *J. Magn. Reson.* **203**, 150 (2010).
- <sup>18</sup>Y. Twig, E. Suhovoy, and A. Blank, *Rev. Sci. Instrum.* **81**, 104703 (2010).
- <sup>19</sup>G. A. Rinard, R. W. Quine, R. T. Song, G. R. Eaton, and S. S. Eaton, *J. Magn. Reson.* **140**, 69 (1999).
- <sup>20</sup>A. Blank and J. H. Freed, *Isr. J. Chem.* **46**, 423 (2006).
- <sup>21</sup>C. P. Poole, *Electron Spin Resonance: a Comprehensive Treatise on Experimental Techniques* (Wiley, New York, 1983).
- <sup>22</sup>B. Blumich, *NMR Imaging of Materials* (Oxford University Press, Oxford, UK, 2000).
- <sup>23</sup>J.-M. Jin, *Electromagnetic Analysis and Design in Magnetic Resonance Imaging* (CRC, Boca Raton, FL, 1999).
- <sup>24</sup>M. S. Conradi, A. N. Garroway, D. G. Cory, and J. B. Miller, *J. Magn. Reson.* **94**, 370 (1991).
- <sup>25</sup>L. Shtirberg and A. Blank, *Concepts in Magnetic Resonance, Part B* (2011) (submitted).
- <sup>26</sup>D. Kajfez and P. Guillon, *Dielectric Resonators* (Artech House, Dedham, MA, 1986).
- <sup>27</sup>R. Halevy, Y. Talmon, and A. Blank, *Appl. Magn. Reson.* **31**, 591 (2007).
- <sup>28</sup>K. J. Liu, G. Bacic, P. J. Hoopes, J. J. Jiang, H. K. Du, L. C. Ou, J. F. Dunn, and H. M. Swartz, *Brain Res.*, **685**, 91 (1995).
- <sup>29</sup>M. Jaworski, A. Sienkiewicz, and C. P. Scholes, *J. Magn. Reson.* **124**, 87 (1997).